Transmission of polarized light in skeletal muscle

Ali Shuaib, Xin Li, and Gang Yao
University of Missouri, Department of Biological Engineering, Columbia, Missouri 65211

Abstract. Experiments were conducted to study polarized light transmission in fresh bovine skeletal muscle of varying thicknesses. Two-dimensional polarization-sensitive transmission images were acquired and analyzed using a numerical parametric fitting algorithm. The total transmittance intensity and degree-of-polarization were calculated for both central ballistic and surrounding scattering regions. Full Mueller matrix images were derived from the raw polarization images and the polar decomposition algorithm was applied to extract polarization parameters. The results suggest that polarized light propagation through skeletal muscle is affected by strong birefringence, diattenuation, multiple scattering induced depolarization and the sarcomere diffraction effect.
© *2011 Society of Photo-Optical Instrumentation Engineers (SPIE)*. [DOI: 10.1117/1.3536512]

1 Introduction

Optical polarization is an intrinsic property of light and actively involved in the light-tissue interactions. Previous studies have demonstrated that optical polarization can provide unique "polarization contrast."[1,2] The polarization state of an incident light can be altered by many different sample's properties such as optical scattering coefficient, absorption coefficient,[3,4] and birefringence.[5] A thorough understanding of the propagation of polarized light in tissue is important for correct interpretation of experimentally measured polarization signals. In a series of studies, Sankaran et al.[6,7] found that the propagation of polarized light may be significantly different in various biological tissues. In this study, we investigated the propagation of polarized light in skeletal muscle tissues, which has not been previously studied in detail.

Skeletal muscles make up to 40% of total human body weight and are responsible for many important physiological functions such as locomotion, body temperature regulation, and serving as a source of nutrient reserve in times of suboptimal dietary intakes. In addition, skeletal muscle's striated relative, cardiac muscle, is critical to life by controlling circulation under a myriad of physiological conditions. Whole muscle consists of fascicles, which are collections of muscle fibers (muscle cells) encapsulated in an elaborate connective tissue matrix. Each muscle fiber consists of thousands of myofibrils. Morphologically, myofibrils are cylindrical structures organized into repetitive units called "sarcomere" which are the fundamental structural and contractile units in striated muscle.[8,9]

Optical methods have been investigated as a noninvasive way to monitor muscle functions *in vivo*.[10,11] Optical absorption properties can reveal changes in chemical compositions such as myoglobin concentrations; whereas optical scattering properties measured in skeletal muscle were correlated with sarcomere length changes.[11] Light propagation in skeletal muscle is quite different from that in isotropic media due to the strong anisotropic structures in muscle.[12,13] Thus a good understanding of light-muscle interaction is needed to interpret optical measurements and develop new optical methods for measuring muscle functions. Our recent studies on polarized reflectance imaging[13] in whole muscle suggest that the propagation of polarized light in skeletal muscle is strongly affected by the sarcomere structures. In this paper, we conducted further studies by analyzing transmittance images in fresh muscle samples of different thicknesses. The polar decomposition algorithm[14–16] was also applied to extract the diattenuation, depolarization, and retardance from the measured Mueller matrix.
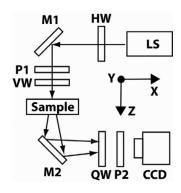
2 Materials and Method

Bovine *Sternomandibularis* muscle was excised from the animal immediately after slaughtering. The thickness of the raw muscle in the relaxed state was approximately 12.0 mm. The muscle sample was prepared by removing surface fat tissues and cut into a small piece of 25.4 mm in length and width. The sample piece was then immersed in a "relaxing solution" (see Refs. 17 and 18 for details) to prevent rigor formation. The sample was kept in the solution during the entire imaging process. To prepare samples of different thicknesses, a small layer was cut gradually from the original sample. The actual sample thickness was measured by using a caliper. The following seven thicknesses were obtained in this study: 12.0, 9.6, 8.7, 6.1, 5.2, 3.7, and 2.7 mm.

The experimental setup is illustrated in Fig. 1. The sample was placed so that the muscle fibers were oriented along the direction of *V*-polarization (*y*-axis in Fig. 1). A polarized He–Ne laser ($\lambda = 632.8$ nm) was used as the light source. The laser light passed through a $\lambda/2$ waveplate (HW) and a polarizer (P1). The incident power was adjusted by rotating the $\lambda/2$ waveplate. A variable waveplate (VW) was used to change the polarization states of the incident light. The transmitted light was imaged by a 16-bit CCD camera with 512×512 pixels (PIXIS 512, Princeton Instruments, NJ) after passing through a $\lambda/4$ waveplate (QW)

Address all correspondence to: Gang Yao, Department of Biological Engineering, University of Missouri, Columbia, MO 65211; E-mail: YaoG@missouri.edu.

Fig. 1 A schematic of experimental setup. LS: a 10 mW He–Ne laser; HW: half waveplate; $M1$, $M2$: mirrors; $P1$, $P2$: polarizers; VW: variable waveplate; QW: quarter waveplate; CCD: imaging camera. A coordinate is setup so that the muscle fiber is oriented along the y-axis and the H-polarization direction is aligned with the x-axis at the sample surface.

and a polarizer (P2). The zoom lens used with the camera had an acceptance angle of 10.5 deg. The image was acquired over an area of 17.5×17.5 mm^2. Thus the acquired image had an actual spatial resolution of 0.034 mm/pixel. To compensate for the signal intensity variation with sample thicknesses and maintain a constant maximum image pixel intensity value, both the CCD exposure time and the incident light power were adjusted during the imaging process. The acquired images were normalized by dividing the recorded incident laser power and CCD exposure time. To improve the signal to noise ratio, 20 images were acquired and averaged to produce the final image at a given condition.

Four different polarization states were used for both incidence and detection in the experiment: horizontal linearly polarized light (H), vertical linearly polarized light (V), linearly polarized light 45 deg to x-axis (P), and right-handed circularly polarized light (R). The system was carefully calibrated[19] and the measured extinction ratio for linearly polarized light and circularly polarized light were >32 and >30 dB, respectively. A total of 16 images were acquired for each sample with different combinations of the four incidence and detection polarizations. For convenience, each acquired image was labeled using two letters: the first term stands for the incident polarization state and the second term stands for the detection polarization state. For example, HV indicates the states with H-polarized incident and V-polarized detection states.

For each incident polarization, the Stokes vector was calculated from the four measurements using different detection polarizations:

$$\mathbf{S} = \begin{pmatrix} S_0 \\ S_1 \\ S_2 \\ S_3 \end{pmatrix} = \begin{pmatrix} I_H + I_V \\ I_H - I_V \\ 2I_P - (I_H + I_V) \\ 2I_R - (I_H + I_V) \end{pmatrix}, \tag{1}$$

where the symbol I_i stands for the transmittance intensity with detection polarization state of i. For example, I_H is the transmittance intensity measured by detecting only H-polarized light.

The full Mueller matrix can be derived from the Stokes vectors measured using four different incidence polarizations:

$$\mathbf{M} = \frac{1}{2} [\mathbf{S}_H + \mathbf{S}_V, \quad \mathbf{S}_H - \mathbf{S}_V, \quad 2\mathbf{S}_P - (\mathbf{S}_H + \mathbf{S}_V),$$
$$2\mathbf{S}_R - (\mathbf{S}_H + \mathbf{S}_V)], \tag{2}$$

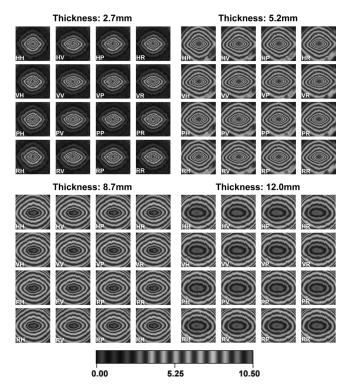where $\mathbf{S}_i$ indicates the Stokes vector for incident light with the polarization state of i. The degree of polarization (DOP), degree of linear polarization (DOLP), and degree of circular polarization (DOCP) of the transmitted light can be calculated from the Stokes vector as:

$$\text{DOP} = \sqrt{\frac{S_1^2 + S_2^2 + S_3^2}{S_0^2}},$$

$$\text{DOLP} = \sqrt{\frac{S_1^2 + S_2^2}{S_0^2}}, \tag{3}$$

$$\text{DOCP} = \left| \frac{S_3}{S_0} \right|.$$

The measured Mueller matrix $\mathbf{M}$ can be represented as the product of three independent matrices representing the Mueller matrices of a diattenuator $\mathbf{M}_D$, a retarder $\mathbf{M}_R$, and a depolarizer $\mathbf{M}_\Delta$: $\mathbf{M} = \mathbf{M}_\Delta \mathbf{M}_R \mathbf{M}_D$. Also, the polar decomposition algorithm[14] can be applied to extract individual polarization

Fig. 2 Transmittance images of different combinations of incident and detection polarizations for muscle samples of: 2.7, 5.2, 8.7, and 12.0 mm thickness. The images were acquired over an area of 17.5×17.5 mm^2. Muscle fiber orientation is along the vertical direction (y-axis) and the H-polarization is along the horizontal direction (x-axis). The images were coded in pseudo-color log-scales as shown in the color-map.

parameters (diattenuation, retardance, and depolarization). The detailed steps have been described elsewhere.[20]

Spatial distributions of the transmission image were studied by analyzing the equi-intensity profiles. In each acquired polarization image, we first extracted all pixels with the same intensity. The coordinates of these pixels were then fitted using the following equation as in our previous studies:[12, 13]

$$\left(\frac{|x|}{a}\right)^q + \left(\frac{|y|}{b}\right)^q = 1, \tag{4}$$

where the parameter q describes the geometrical shape of the equi-intensity profile with $q = 1$ indicating a rhombus and $q = 2$ indicating an ellipse. The parameters a and b indicate the axis length along the x- and y-axis, respectively. The ratio of the two axes, which we defined as the B parameter, was calculated as:
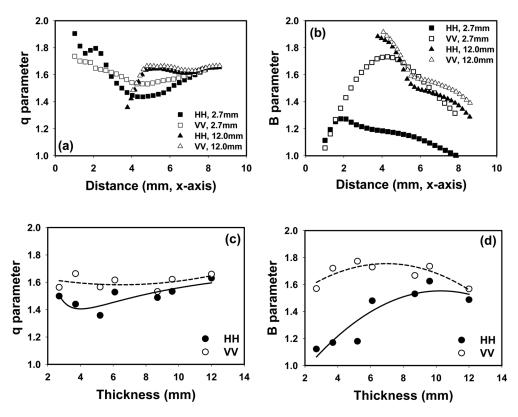
$$B = \frac{a}{b}. \tag{5}$$

3 Results and Discussions

3.1 Spatial Profiles of the Transmittance Images

Figure 2 shows the 16 transmittance images measured with different combinations of incidence and detection polarization states. Results shown were obtained in muscle samples of 2.7, 5.2, 8.7, and 12.0 mm thickness. The muscle fiber was oriented along the vertical direction (y-axis) that was aligned with vertical polarization on the sample surface. The equi-intensity

images were drawn using a pseudo-color scale with the same color standing for the same intensity.

In the thin sample (2.7 mm thick), variations in spatial profiles can be seen in different polarization images. Specifically, the *VV* image was elongated along the x-axis; while the *HH* image was somewhat equally distributed along the x- and y-axis. Other images showed geometric distributions somewhere in between the *HH* and *VV* images. Such shape difference in the equi-intensity profiles gradually disappeared in samples of larger thicknesses. As shown in Fig. 2, the polarization images obtained in a 12.0 mm thick sample were nearly identical.

The rhombus-shaped equi-intensity profiles in Fig. 2 were similar to those observed in muscle reflectance images.[12, 13] Such unique profiles were clearly different from the circular profiles in an isotropic medium and the elliptical profiles in a fibrous sample.[21] To quantify the equi-intensity profiles, Eq. (4) was used to fit all acquired raw polarization images. The results confirmed the observation in Fig. 2 that the equi-intensity profiles in *HH* and *VV* images represented two extreme cases and other images had profiles between them. In addition, the shapes of the equi-intensity profiles showed dependency on the evaluation distance from the incident point. In the 2.7 mm thick sample, the fitted q values were ∼1.8 at ∼1.0 mm to the incident point and decreased thereafter with the distance [Fig. 3(a)]. It reached the minimal at ∼4.0 mm to the incident point and started to increase thereafter. At larger distances (∼8 mm) from the incident point, the fitted q values were ∼1.6, identical in *HH* and *VV* images; while the *VV* image had higher q values than the *HH* image at distances between 3–7 mm from the incident point.

Fig. 3 Fitted (a) q and (b) B parameters at varying distances from the incident point measured in *HH* and *VV* images obtained for muscle samples of 2.7 and 12.0 mm thickness. At a fixed distance of 6 mm from the incident point, graphs (c) and (d) show the fitted q and B parameters in muscle samples of different thicknesses.

These results are consistent with the observation (Fig. 2) that the equi-intensity profile in the HH image appeared closer to a rhombus. In the 12 mm sample, the equi-intensity profiles at small distances (<4 mm) were irregular. However, the fitted q values were stable starting at 4 mm from the incident point, and the HH and VV images had essentially the same q values.

In the 2.7 mm thick sample, the fitted B values were very different in the HH and VV images except for those measured at small distances [Fig. 3(b)]. The fitted B values approached 1.0 in both HH and VV images when measured at distances close to the incident point (∼1 mm). Taking into consideration a large fitted q value [Fig. 3(a)], these results indicated a circular beam profile with close agreement with the incident beam profile, suggesting a dominant component of nonscattered light. At distances larger than 2 mm, the fitted B values in the VV image were significantly larger than those in the HH image [Fig. 3(b)]. In other words, the equi-intensity profiles in the VV image were more elongated along the x-axis (perpendicular to muscle fibers). In both HH and VV images, the fitted B values initially increased with distance, reached a maximal value, and thereafter decreased with distance. Therefore, the equi-intensity profile became less anisotropic at large distances from the incident point.

The fitted B parameters were similar in the HH and VV images obtained in the 12 mm thick sample [Fig. 3(b)]. Considering the similar fitted q values, this suggested that the equi-intensity profiles had almost identical shapes in the HH and VV images in the 12 mm thick sample. The fitted B values decreased from ∼1.9 at 4.0 mm distance to ∼1.4 at 8.5 mm distance, suggesting the profile became less elongated along the x-axis (perpendicular to muscle fibers) with the evaluation distance.
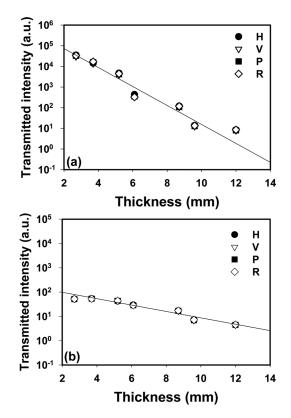
Figures 3(c) and 3(d) show the fitted q and B parameters obtained in samples of different thicknesses. The values were measured at a fixed distance of 6 mm from the incident point where the fitting parameters were relatively stable with distance. Overall, the fitted q parameters had small variations between 1.4–1.7 in samples of 2.7–12 mm thick, indicating a nonelliptical distribution. In addition, the larger than 1.0 B parameters confirmed the observation in Fig. 2 that equi-intensity profiles were elongated perpendicular to muscle fiber orientations even at larger distances from the incident point in thick samples. This was in sharp contrast with that observed in nonmuscle fibrous samples where equi-intensity profiles were elongated parallel to the fiber orientation at larger distances.[21] This phenomenon suggested light propagation behavior in muscle was different from that in fibrous samples. Because the periodic sarcomere structure is the most distinct feature of striated muscles comparing with non-muscle fibrous tissues, the strong sarcomere diffraction[22] most likely have played certain roles in modulating light propagation in skeletal muscle.

Moreover, the B parameter was much smaller in the HH image than in the VV image at small thicknesses. In other words, the optical transmission was more symmetric along the x and y directions in the HH images. At small sample thicknesses, the transmitted light contained a significant portion of light that only experienced a few times of scattering. On the one hand, the incident light may be scattered by cylindrical fibers to directions that were perpendicular to the fiber orientation.[21] On the other hand, the incident light may also be diffracted by the periodic sarcomere structure to directions that were parallel to the fiber orientation.[22] These two competing effects likely "stretched" the

transmitted light along both the x- and y-axis, resulting in the patterns shown in thin samples. Our previous calculation has shown that the periodic sarcomere structure[13] diffracts much less V-polarized light along the muscle fibers than H-polarized light. Therefore, the scattering toward the x-axis overpowered that toward the y-axis in the VV image, which was confirmed by the higher B values in VV (Fig. 3). It is worth mentioning that photons could also experience Mie scatterings by tissue constituents such as cell nuclei. Such Mie scatterings scatter more linearly polarized light to the orthogonal directions.[13] It is likely that both mechanisms contributed to the difference equi-intensity distributions in HH and VV images. However, the difference in both q and B values between HH and VV images diminished with sample thickness due to depolarization caused by multiple scatterings.

3.2 *Intensity Change with Thickness*

Overall, the transmitted light intensity decreased with sample thickness as in other tissues. As shown in Fig. 2, the transmitted light covered a large area even with a point incident light beam. To quantitatively study the change of transmission with sample thickness, we divided the image area into two regions: the first "central" region covered an area with a radius of 15 pixels (∼0.5 mm) from the incident point, roughly the same size as the incident beam; and the second "scattering" region covered an

Fig. 4 The unpolarized total transmitted intensity measured with different incident polarization states in samples of different thickness. (a) Intensity averaged within a 1 mm (30 pixels) diameter from the incident point minus the extrapolated scattering component values within the region. (b) Intensity averaged within an area that is between 2.05 mm (60 pixels) and 6.84 mm (200 pixels) from the incident point (scattering region). The lines in the graph are exponential fitting results.

area with radii between 60 and 200 pixels (2.05–6.84 mm) from the incident point. The transmitted light intensity was calculated by averaging pixel counts with the specific region. All intensities were normalized by dividing the exposure time and the incident power for the corresponding incident polarization.
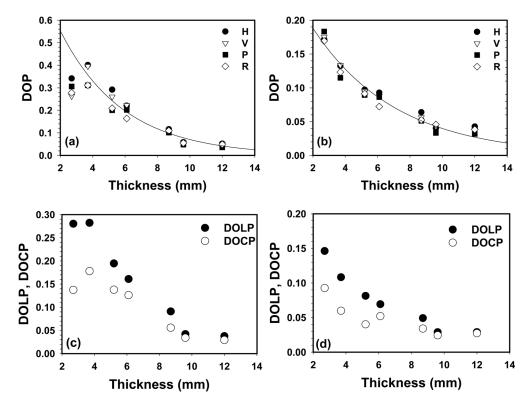
Because of the small incidence beam size (∼1 mm), transmitted light in the second region must be scattered. On the other hand, transmitted light within the central region may consist of both nonscattered and scattered components. The scattered component increased with thickness. To improve the estimation of the nonscattered components within the central region, the transmittance within the second region was fitted with a two-dimensional Gaussian function which was extrapolated to the central region to estimate the scattered component. The extrapolated values were then deducted from the intensities measured within the central region. We found the scattered component was only significant at the last two thicknesses (9.7 and 12.0 mm) within the central region [Fig. 4(a)].

As shown in Fig. 4, the central transmittance decreased nearly exponentially with the sample thickness. The fitted attenuation coefficient was 1.06 mm^{-1} ($R^2 = 0.95$). The transmittance in the second (scattering) region had little change in the intensities up to ∼5 mm thickness. Then, it started to decrease exponentially, but at a much slower rate of 0.30 mm^{-1} ($R^2 = 0.96$, without the data at 2.7 mm). Due to the thin thickness, there was not much multiply scattered light at 2.7 mm and thus this data point did not follow the exponential trend [Fig. 4(b)] obtained from thicker samples. At ∼10 mm thickness, the optical

intensity at the central region became similar to that in the second (scattering) region. This was in general agreement with intensity decay profiles in any scattering media where ballistic light experiences a much higher attenuation rate than multiply scattered light because of the "ballistic" path constraint (i.e., following the original incident direction).
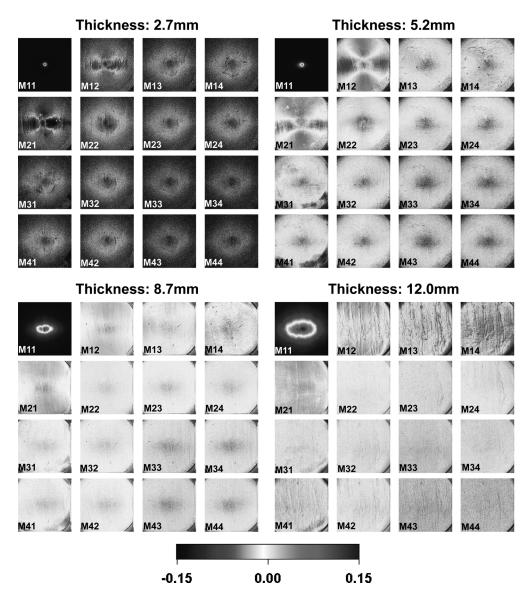
3.3 Optical Polarization Changes with Sample Thickness

Figures 5(a) and 5(b) show the measured DOP in samples of different thicknesses. Similarly to Fig. 4, the results were calculated separately in the central region and the scattering region. The DOP decreased almost exponentially. There was no significant difference among the results obtained using incident light with different polarization states. However, the DOP of the ballistic component (central region) decreased much faster than the scattered component. The fitted decay rates were 0.26 and 0.19 mm^{-1} for the central (ballistic) and scattered components, respectively. The two fitting curves converged to a low value of ∼0.02 at large sample thickness (∼14 mm). To be noted, these DOP decay rates were smaller than those of the light intensities (Fig. 4), suggesting the decrease of DOP was slower than the intensity attenuation. Because transmitted light in the central region contained nonscattered photons and photons with a few scatterings, its DOP remained higher than those in the scattering region. At large thickness, even photons transmitting from the

Fig. 5 The DOP change with sample thickness presented for each measured incident polarization state. (a) Results averaged within 1 mm (30 pixels) diameter from the incident point. (b) Results averaged within an area that is between 2.05 mm (60 pixels) and 6.84 mm (200 pixels) from the incident point. The lines in graphs (a) and (b) are exponential fitting results. For *H*-polarized incident light, the DOLP and DOCP were calculated and shown in (c) by measuring light within 1 mm (30 pixels) diameter from the incident point, and (d) by measuring light within an area that is between 2.05 mm (60 pixels) and 6.84 mm (200 pixels) from the incident point.
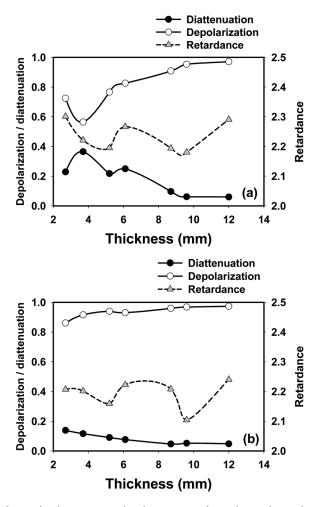
Fig. 6 The transmission Mueller matrix images derived from the polarization images in Fig. 2 obtained for muscle samples of 2.7, 5.2, 8.7, and 12.0 mm thickness. The image shown has a size of 17.5×17.5 mm^2. The muscle fiber is oriented along the vertical direction (y-axis) and the H-polarization is along the horizontal direction (x-axis). The Mueller matrix images are normalized against M_{11}.

central region were likely multiply scattered, thus their DOP values were similar to those transmitting from scattering region.

Figures 5(c) and 5(d) show the DOLP and DOCP for H-polarized incident light measured in samples of different thicknesses. They followed a similar decrease trend with sample thickness as the total DOP as shown in Figs. 5(a) and 5(b). It is interesting to note that circular polarization can be detected although the incident light was linearly polarized, most likely due to birefringence of muscle fibers. The DOCP value was smaller than the corresponding DOLP value, which was also observed in other biological tissues.[6,7] However, the difference diminished at larger sample thicknesses ($\sim$10 mm).

Figure 6 shows the Mueller matrix images calculated from the raw images (Fig. 2) using Eq. (2). In the 2.7- and 5.2-mm thick sample, M_{12} and M_{21} elements clearly showed crosslike patterns as observed in our previous reflectance measurements.[13] However, no clear patterns were seen in the Mueller matrix images in thick samples. All elements (except for M_{11}) were

essentially blank images with values close to zero. This typical depolarization Mueller matrix visualized that the transmitted light was fully depolarized after passing through a thick muscle sample.

Figure 7 shows the diattenuation, depolarization, and retardance in samples of different thicknesses extracted using the Polar decomposition algorithm. The calculation was conducted separately in the central and scattering regions and the results represented an overall assessment of the whole sample in a specific region. As expected, birefringence existed in muscle samples. The calculated retardance appeared to fluctuate between 2.1 and 2.3 with sample thickness and had a slightly higher value in the central region. As a contrast, the depolarization and diattenuation showed a clear trend with thickness. The depolarization was higher in the scattering region than in the central region. It increased with tissue thickness from $\sim$0.56 to $\sim$0.97 and from $\sim$0.86 to $\sim$0.97 in the central and scattering regions, respectively. These changes were consistent with the

Fig. 7 The diattenuation, depolarization, and retardance obtained using polar decomposition in samples of different thicknesses. (a) Results averaged within 1 mm (30 pixels) diameter from the incident point. (b) Results averaged within an area that is between 2.05 mm (60 pixels) and 6.84 mm (200 pixels) from the incident point.

degree-of-polarization shown in Fig. 5. Polar decomposition also revealed significant diattenuation in the muscle with higher values in the central region than in the scattering region. The obtained diattenuation decreased with thickness from ∼0.36 to ∼0.06 in the central region and from ∼0.14 to ∼0.05 in the scattering region, respectively.

4 Conclusion

The polarization-sensitive transmittance images in fresh bovine muscle with different thicknesses were acquired with a point-incident light beam. The two-dimensional equi-intensity profiles of the transmission light had rhombuslike shapes that were in between the circular pattern observed for isotropic scattering media and the elliptical pattern observed for fibrous sample scattering. This unique geometrical shape can be characterized by the q-parameter [Eq. (4)] which varied only slightly with sample thickness when evaluated at a distance away from the incident point. The other shape parameter, B, showed strong dependency on incident polarization, which was likely related to polarization-dependent sarcomere diffraction as discussed in Sec. 3.1. The non-polarized transmittance intensity showed

exponential decay with sample thickness as in any turbid media. The multiple-scattering effect was clearly shown in the reduced DOP values with sample thickness. The degree of linear polarization was consistently larger than the degree of circular polarization. In addition, polar decomposition of the Mueller matrix indicated that muscle tissue had strong diattenuation in addition to birefringence. As skeletal muscles are one of the most abundant tissues in humans as well as in animals, these results may provide useful information for the study of light-muscle interactions.

References

1. S. L. Jacques, J. C. Ramella-Roman, and K. Lee, "Imaging skin pathology with polarized light," *J. Biomed. Opt.* **7**(3), 329–340 (2002).
2. S. L. Jacques, J. R. Roman, and K. Lee, "Imaging superficial tissues with polarized light," *Lasers Surg. Med.* **26**, 119–129 (2000).
3. R. Nothdurft and G. Yao, "Expression of target optical properties in subsurface polarization-gated imaging," *Opt. Express* **13**(11), 4185–4195 (2005).
4. R. Nothdurft and G. Yao, "Applying the polarization memory effect in polarization-gated subsurface imaging," *Opt. Express* **14**(11), 4656–4661 (2006).
5. J. J. Pasquesi, S. C. Schlachter, M. D. Boppart, E. Chaney, S. J. Kaufman, and S. A. Boppart, "*In vivo* detection of exercised-induced ultrastructural changes in genetically-altered murine skeletal muscle using polarization-sensitive optical coherence tomography," *Opt. Express* **14**(4), 1547–1556 (2006).
6. V. Sankaran, J. J. T. Walsh, and D. J. Maitland, "Polarized light propagation through tissue phantoms containing densely packed scatterers," *Opt. Lett.* **25**(4), 239–241 (2000).
7. V. Sankaran, J. Joseph, T. Walsh, and D. J. Maitland, "Comparative study of polarized light propagation in biologic tissues," *J. Biomed. Opt.* **7**(3), 300–306 (2002).
8. C. G. Bönnemann and N. G. Laing, "Myopathies resulting from mutations in sarcomeric proteins," *Curr. Opin. Neurol.* **17**(5), 529–537 (2004).
9. M. Ferrai, T. Binzoni and V. Quaresima, "Oxidative metabolism in muscle," *Phyl. Trans. R. Soc. Lond. B* **352**, 677–683 (1997).
10. G. Yu, T. Durduran, G. Lech, C. Zhou, B. Chance, E. R. Mohler Iii, and A. G. Yodh, "Time-dependent blood flow and oxygenation in human skeletal muscles measured with noninvasive near-infrared diffuse optical spectroscopies," *J. Biomed. Opt.* **10**(2), 024027 (2005).
11. J. Xia, A. Weaver, D. E. Gerrard, and G. Yao, "Monitoring sarcomere structure changes in whole muscle using diffuse light reflectance," *J. Biomed. Opt.* **11**(4), 040504 (2006).
12. J. Ranasinghesagara and G. Yao, "Imaging 2D optical diffuse reflectance in skeletal muscle," *Opt. Express* **15**(7), 3998–4007 (2007).
13. X. Li, J. C. Ranasinghesagara, and G. Yao, "Polarization-sensitive reflectance imaging in skeletal muscle," *Opt. Express* **16**(13), 9927–9935 (2008).
14. S. Y. Lu and R. Chipman, "Interpretation of Mueller matrices based on polar decomposition," *J. Opt. Soc. Am. A* **13**(5), 1106–1113 (1996).
15. S. Manhas, M. K. Swami, P. Buddhiwant, N. Ghosh, P. K. Gupta, and J. Singh, "Mueller matrix approach for determination of optical rotation in chiral turbid media in backscattering geometry," *Opt. Express* **14**(1), 190–202 (2006).
16. N. Ghosh, M. F. G. Wood, and I. A. Vitkin, "Mueller matrix decomposition for extraction of individual polarization parameters from complex turbid media exhibiting multiple scattering, optical activity, and linear birefringence," *J. Biomed. Opt.* **13**(4), 044036 (2008).
17. K. S. McDonald, M. R. Wolff, and R. L. Moss, "Force-velocity and power-load curves in rat skinned cardiac myocytes," *J. Physiol.* **511**(2), 519–531 (1998).

18. K. Tawada and M. Kimura, "Stiffness of carbodiimide-crosslinked glyc-erinated muscle fibres in rigor and relaxing solutions at high salt con-centrations," *J Muscle Res. Cell Motil.* **7**(4), 339–350 (1986).

19. J. S. Baba, J. R. Chung, A. H. DeLaughter, B. D. Cameron, and G. L. Cote, "Development and calibration of an automated Mueller matrix polarization imaging system," *J. Biomed. Opt.* **7**(3), 341–349 (2002).

20. X. Li and G. Yao, "Mueller matrix decomposition of diffuse reflectance imaging in skeletal muscle," *Appl. Opt.* **48**(14), 2625–2631 (2009).

21. A. Shuaib and G. Yao, "Equi-intensity distribution of optical reflectance in a fibrous turbid medium," *Appl. Opt.* **49**(5), 838–844 (2010).

22. J. Ranasinghesagara and G. Yao, "Effects of inhomogeneous myofibril morphology on optical diffraction in single muscle fibers," *J. Opt. Soc. Am. A* **25**(12), 3051–3058 (2008).